International Journal of Fluid Dynamics (2002) **Vol 6**, Article 1, 1–15
Available online at: http://elecpress.monash.edu.au/ijfd

The Flow Patterns in Two Immiscible Stratified Liquids Induced by Bubble Plume

Hassan Abdulmouti
Department of Mechanical Engineering, Fukui University, Bunkyo 3-9-1, Fukui 910-8507, Japan.

Keywords: Multiphase Flow, Bubble Plume, Surface Flow, Flow Visualization, Stratified Liquid, Particle Image Velocimetry (PIV)

(Received May 15 2002, and in revised form September 4 2002.
Publication date December 27 2002.)

The bubble plume is known as one of the transport phenomena able to drive a large-scale convection due to the buoyancy of bubbles. We presented the fundamental characteristics of the surface flow generation mechanism in an earlier paper. The technique of using a surface flow generated by a bubble plume is proposed as a means of collecting the surface-floating substances, especially the oil layer, during large oil-leakage accidents in order to protect naval systems, rivers, and lakes. However, in the past there have been no reports concerning the interaction mechanism between the surface flow generated by the bubbles and the oil layer as an application to an actual oil fence. Laboratory experiments have been carried out in order to investigate the multi-dimensional transportation of oil due to bubbles. The liquid flow pattern of bubble-induced convection in a stratified liquid is clarified by using particle imaging velocimetry (PIV) measurement and pathline measurements. Furthermore, the mixing effect of the oil layer is elucidated by using image processing and flow visualization in order to improve the system performance. On the other hand, the altitude of the upheaval bulge of the interface of the two-phase stratified liquids induced by the bubble plume, which is a very important factor in breaking the oil layer, is measured experimentally and calculated theoretically. The experimental results resemble the theoretical results.

NOMENCLATURE

A	area of calculation in the injector region, (injector surface of the bubble generator).
cc	cross-correlation coefficient (for mixing effect).
g	gravitational acceleration.
D	equivalent (mean) bubble diameter.
$H_{\text{oil}} = h_2$	initial height of the oil layer.
Q_g	gas volume flow rate.
Q_g^*	dimensionless parameter defined by equation (1).
Q_l	liquid volume flux.
v_b	rising bubble velocity.
w	width of the jet or the bubble plume.
α	void fraction.
δ	thickness (width) of the experimental tank.
Δh	distance between the initial water level and the top position of the upheaval water (the altitude of the upheaval bulge of the interface of the stratified two-phase liquids induced by the bubble plume).
ν_{oil}	kinematic viscosity of the oil.
ϕ_1	brightness of the first image (without bubble).
ϕ_2	brightness of the second image.
ρ_1	density of the first layer (water).
ρ_2	density of the second layer (silicone oil).

1. INTRODUCTION

A bubble plume is observed in various engineering disciplines, e.g. in industrial, material, chemical, mechanical, and environmental applications such as chemical plants, nuclear power plants, naval engineering, accumulation of the surface slug in the metal refining process, the reduction of surfactants in chemical reactive processes, waste treatment, gas mixing and resolution, heat and mass transfer, aeronautical and astronautical systems, biochemical reactors as well as distillation plants and so on. On the other hand, the improvement and development in the performance of oil barriers (oil fences) is required especially for high values of current velocity, wave height and wind velocity in order to protect the environment and the naval plants from oil pollution. Hence, a bubble plume is considered to possibly be an effective way to control the density and transportation of surface-floating substances, and it is expected to be an effective tool to support the function of an oil fence since it can generate a strong and wide surface flow over the bubble generation system, and it can damp the wave motion. Many researchers have carried out extensive model experiments by focusing on the flow field using air bubbles because gas injection through a bottom nozzle is the most popular and has wide applications. Since bubble plumes have been used with varying degrees of success more information on these subjects should be accumulated (Abdulmouti *et al.* 2001, Gross & Kuhlman 1992, Sun & Faeth 1986 a,b, Hussain & Narang 1984, Hara, Ikai, & Namie 1984, Chesters, Van Doorn & Goossens 1980, McDougall 1978, Abdel-Aal, Stiles & Holland 1966).

Bilayer convection is an interesting transport process to be studied for both theoretical and applied reasons. Theoretically, a bilayer convection is full of nonlinear dynamics with a wide range of parameters to be investigated. There are many applications for bilayer

convection; the most important one is the oil fence application. Two-layer systems have been studied theoretically and experimentally by many researchers. Degen *et al.* (1998) has studied two-layers heated from below experimentally. Johnson *et al.* (1997) presented a brief review of convective phenomena associated with material processing, and they explained several instability phenomena that can occur in a bilayer of two fluids heated from either the top or the bottom and the effect of laterally and vertically confined geometries. Johnson & Narayanan (1998), and Renardy & Stoltz (2000) discussed Marangoni effects and studied purely buoyancy driven convection for specific two-layer systems. They also investigated the velocity vectors of a water silicone oil system in thermal convection. The presence of the interface and the coupling between the fluids has received attention by both experimentalists and theoreticians. However, in the past there have been no reports concerning the calculation of the altitude Δh of the upheaval bulge of the two-phase stratified liquid interface, which is induced by a bubble plume. This parameter is a very important factor in breaking the oil layer. Hence it is very important to calculate this parameter.

It is well known that bubbly flows show a complicated behavior due to the strong dynamic interaction between bubble and vortex motions. Although the bubbly flow mechanism and the fundamental characteristics of the surface flow generation mechanism which is induced by the bubble plume were described in our earlier paper (Abdulmouti *et al.* 2001), the flow structure inside the two-phase stratified liquids has not yet been made clear. The motivation of the present work is the demand to know the separation mechanism of oil due to bubbling and the flow pattern inside the stratified two-phase liquids. Considering applications, our aim is to focus on the actual oil transportation effect considering an oil layer on a free surface. In the present study, the oil transportation phenomenon due to the bubble plume is introduced. The experimental measurement of the oil-water interface motion using image processing is presented. Then the flow structure of the bubble-induced convection in a stratified liquid is clarified by using PIV measurements and pathline measurements. Moreover, the mixing effect of oil layer is explained by using image processing and flow visualization in order to improve the system performance. On the other hand, the altitude of the upheaval bulge of the interface between two-phase stratified liquids, which is induced by the bubble plume and which depends on the bubbling conditions (such as gas flow rate, bubble radius and void fraction), is measured experimentally and calculated theoretically. The experimental results show similarity to the theoretical results.

2. EXPERIMENTAL APPARATUS AND CONDITIONS

An experimental apparatus for investigating the interaction between the surface flow generated by bubbles and the oil layer is constructed as shown in Figure 1. The tank is 500 mm in length, 750 mm in height, and 24 mm wide. The stratified liquid in the tank, which consists of water and silicone oil, stands 500 mm high. The initial height of the water layer is $h_1 = 350$ mm and that of the oil is $h_2 = 150$ mm. The experimental conditions of the two layers are summarized in Table 1. The density of the oil is about 10% lighter than that of the water, and the kinematic viscosity of the oil is ten times that of water. These conditions are selected to be similar to heavy oil in the sea. The bubble generator consists of 110 needles, each needle is 0.15 mm in diameter, installed at the bottom of the tank. The injector surface of the bubble generator is the area $A = 55 \times 22$ mm. The gas flow rate is precisely controlled by a pressure regulator and a flowmeter. A lighting setup

with a black background and metal halide lamps is used for taking pathline images and PIV measurements. A white background and metal halide lamps are used for other steps of image processing. The visualized flows are recorded by a digital video camera (Sony, DCR-VX1000) that captures 30 fps. The digital images are preprocessed through the NIH image software version 1.60 (produced by the National Institutes of Health of the United States of America). The preprocessing entails sharpening, binarizing and smoothing of the images. In this paper, the horizontal direction is considered to be the x direction, and the y direction is the vertical direction centered in the bubble plume. The point of origin of the x–y coordinate system is located at the center of the bubble generator as shown in Figure 1. The bubble injector conditions are shown in Table 2, the values in this table are calculated by using the time average of 120 consecutive frames in the image processing (4 seconds). In Table 2, Q_g^* is a dimensionless parameter defined by Eq. (1).

$$Q_g^* = \frac{Q_g}{H_{\text{oil}} v_{\text{oil}}} \tag{1}$$

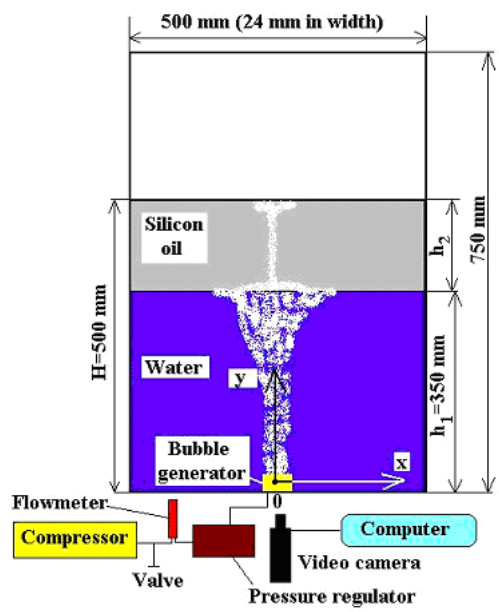

Figure 1. Schematic diagram of experimental apparatus.

The averaged bubble diameter and the standard deviation are calculated by measuring more than 1200 bubbles in the local VTR images in the bubble plume using image processing. These images are taken by recording local pictures of the injector region of the bubble generator. The bubble diameter is defined by the equivalent bubble diameter using ellipsoidal approximations for the bubble shapes. The equivalent bubble diameter is estimated by the vertical and the horizontal lengths of each bubble, which are obtained by using the NIH software after binarizing the images. The measurement uncertainty for the bubble diameter is estimated to be around (0.01 mm) according to the pixel resolution. The

Parameter	Value
Density of water	ρ_1=1000 kg/m^3
Kinematic viscosity of water	$\nu = 10^{-6}$ m^2/s
Density of silicone oil	$\rho_2 = 935$ kg/m^3
Kinematic viscosity of oil	$\nu_{\rm oil} = 10^{-5}$ m^2/s
Temperature of environment	12–20 °C
Maximum gas flow rate	20.0×10^{-6} m^3/s

TABLE 1

Experimental conditions of the two layers.

void fraction (α) is calculated by using the equation ($\alpha = Q_g/A \times v_b$) (Kataoka *et al.* 1993, Murai & Matsumoto 1998, Matsumoto & Murai 1995, Murai & Matsumoto 1999, Murai *et al.* 2001). The measurement uncertainty for the void fraction is estimated to be about 3%.

Gas flow rate Q_g m^3/s)	Non-dimensional flow rate Q_g^*	Mean bubble diameter D (mm)	Standard deviation of D (mm)	Void fraction α
0.28×10^{-6}	0.185	0.70	0.010	0.020
1.39×10^{-6}	0.926	0.80	0.015	0.035
2.78×10^{-6}	1.852	0.95	0.030	0.050
4.17×10^{-6}	2.778	1.10	0.040	0.070
5.56×10^{-6}	3.707	1.25	0.045	0.090
6.94×10^{-6}	4.630	1.40	0.055	0.105
8.33×10^{-6}	5.556	1.60	0.060	0.115
$9.72 \times 10^{-}6$	6.481	1.80	0.070	0.130
11.11×10^{-6}	7.407	2.00	0.085	0.145
12.50×10^{-6}	8.333	2.30	0.095	0.160
13.89×10^{-6}	9.259	2.55	0.100	0.180
15.28×10^{-6}	10.185	2.80	0.110	0.190
16.67×10^{-6}	11.111	3.00	0.120	0.200

TABLE 2

The bubble injector conditions.

3. EXPERIMENTAL RESULTS

(a) Visualization of The Flow Pattern Inside the Two Layers

In order to clarify the flow pattern of the internal liquid flow (the flow field around the bubble plume), spherical particles made of a highly-porous polymer with diameters of 200 to 600 μm and a density of 1010 kg/m^3, are used as tracer particles for both the pathlines and the PIV measurements. The traceability of these particles against the flow in the oil layer is estimated theoretically by using the equation of translational motion of spherical particles. In this equation, the inertial force of the particle, the drag forces from liquid and gas phases, and the added inertial forces of the two phases are all considered. On the other hand, the value of the velocity of the particles to that of the oil liquid is calculated to be more than 97%. Using these estimations, it has been confirmed that the particles sufficiently follow the flow in the oil layer when the frequency of the velocity fluctuation

is lower than 20 Hz. Figure 2 shows samples of the recorded images of the flow field around a bubble plume. In these images the bubble plume is located in the middle of the image, while the particles are distributed around the bubble plume. Our observation showed that the particles and the bubbles have an almost two-dimensional motion in the x–y plane. The time-averaged flow is almost two-dimensional especially because the tank width is small and there are no perpendicular components to the front and back walls in the time-averaged flow field. Hence, a two-dimensional measurement using PIV and pathlines is helpful for grasping the time-averaged internal flow structure. The images are ported to a computer, and the pathlines are calculated for 60 consecutive frames (2 seconds) averaging the movement of the particles after preprocessing the digital images through the NIH software as shown in Figure 3. Moreover, the time-averaged velocity vector map is obtained by using the BDCC (Brightness Distribution Cross-Correlation) method (Gross & Kuhlman 1992) $Q_g = 0.28 \times 10^{-6}$ m^3/s as shown in Figure 4 (which represents the two-phase flow pattern). Although the PIV velocity vectors obtained may be of the gas-liquid interfaces rather than the liquid, it is thought reasonable to assume that in the plume the liquid velocity is the same as the bubble velocity.This result is obtained by using more than 250000 velocity vectors, which are captured during 120 consecutive image frames (4 seconds). The grid-averaging method is used in order to get a grid-rearranged vector map. Then, the stream function is calculated and the streamlines are drawn as shown in Figure 5. However the oil-water interface is not clearly visible in this part of the experiment and the velocity components in the two-phase region cannot be extracted from this image due to the limitation in the pixel resolution; it is not clear which is the resultant velocity vector in this region. Detailed measurements of the oil-water interface are therefore carried out by another experiment and will be explained later. In this section only the macroscopic flow pattern is discussed.

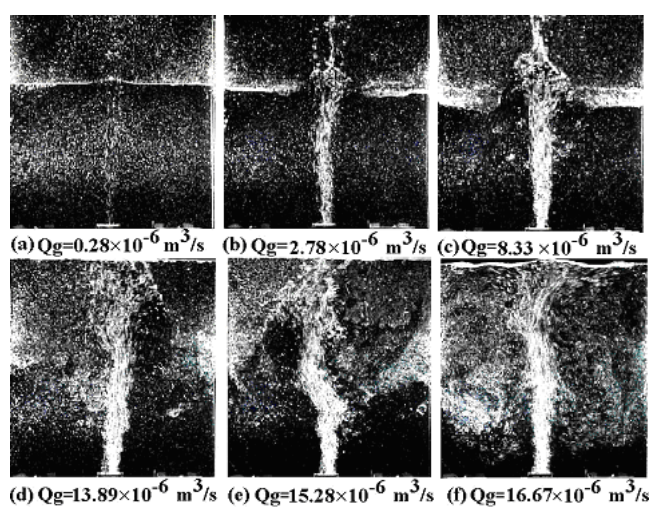

Figure 2. Samples of the recorded images at various gas volume flow rates.

According to these figures the detailed flow mechanism inside the two layers can be explained as follows.

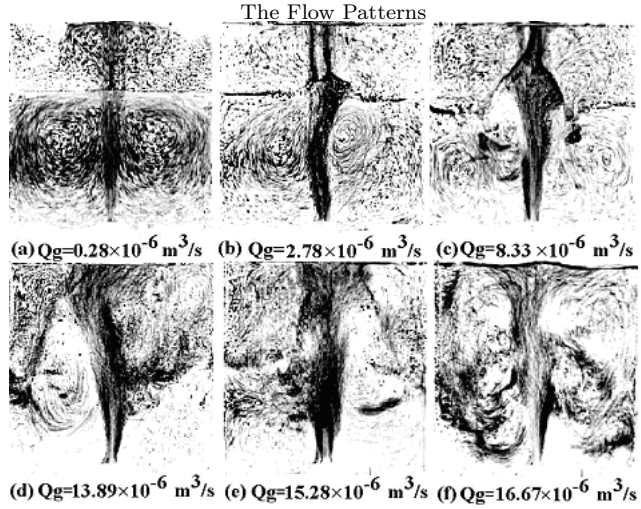

Figure 3. The pathlines of the flow pattern at various gas volume flow rates.

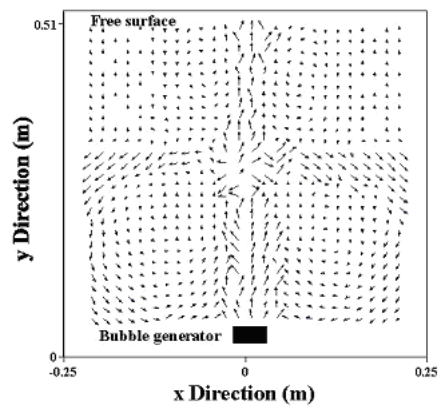

Figure 4. Velocity vector map of the flow pattern for $Q_g = 0.28 \times 10^{-6}$ m^3/s.

(1) The flow is steady and symmetric to the bubble plume when a small gas flow rate is given as shown in Figure 3 (a), (b), (c), the main upward liquid flow in the water layer is driven along the bubble plume by the rising bubbles. The momentum of the upward flow becomes maximum near the oil-water interface. Just under the oil-water interface the upward flow changes its orientation rapidly into a horizontal flow. Then, in the water layer a pair of liquid circulations is generated besides the bubble plume. After time passes by, the pair of circulations induces a whole scale circulation in the entire water layer. At the same time, some bubbles accumulate on the oil-water interface. Beyond that, a part of the bubble plume penetrates and passes the oil stratum causing a secondary flow inside the oil layer by the buoyancy of the penetrating bubble. The velocity of the penetrating bubbles inside the oil layer is less than that

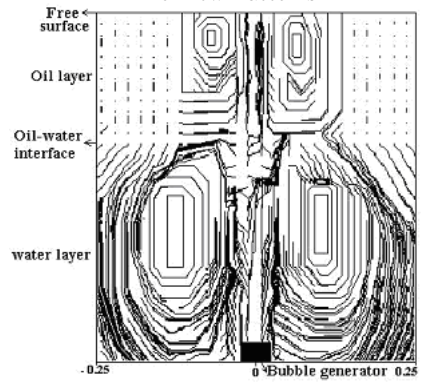

Figure 5. Streamlines obtained by PIV for $Q_g = 0.28 \times 10^{-6}$ m^3/s.

induced inside the water layer due to the high oil viscosity. Thus, the velocity of the bubbles decreases quickly when they enter the oil layer. Therefore, the void fraction inside the oil layer increases. The detailed mechanism of generating the secondary flow inside the oil layer (which is similar to that induced in the water layer) can be explained as follows: A secondary main upward liquid flow of the oil layer is driven by the rising penetrating bubbles along the bubble plume. The momentum of this upward flow becomes maximum (of its values in the oil layer) near the free surface (but still smaller than that induced in the vicinity of the oil-water interface). Just under the free surface the upward flow inside the oil layer changes its orientation into a horizontal flow. Then, another secondary pair of liquid circulations is generated in the oil layer besides the bubble plume. Around this pair of circulations, the accumulated bubbles on the oil-water interface slowly rise through the oil layer to the free surface and float. However, the pair of circulations inside the oil layer is smaller than that induced inside the water layer due to the effect of the oil viscosity. Hence, the surface flow induced by the bubbles inside the oil layer at the free surface is weaker and smaller in scale than that induced inside the water layer in the vicinity of the oil-water interface.

(2) When a large gas flow rate is given as shown in Figure 3 (d), (e), the flow pattern around the bubble plume is quite different from the previous cases, i.e. no pairs of circulations around the bubble plume occur since the oil and water layers start to mix with each other and the flow becomes unsteady, resulting deformations in this area. Furthermore, a strong vortex motion is induced. This vortex motion plays a role generating strong shear stress near the oil-water interface and achieves the penetration of water inside the oil layer.

(3) The vortex motion becomes clearer when a larger gas flow rate is given as in Figure 3 (f) where all liquid is a mixture of water and oil and the flow pattern is complex and unsteady. Here, inside the entire tank a pair of circulations of the mixed liquid around the bubble plume is induced.

In order to clarify the detailed structure of the flow in the two layers, the two-dimensional distribution of the kinetic energy is calculated from the measured averaged velocity vector map as shown in Figure 6. This shows that the highest kinetic energy is generated at a long distance in the center of the bubble plume and in the vicinity of the oil-water interface.

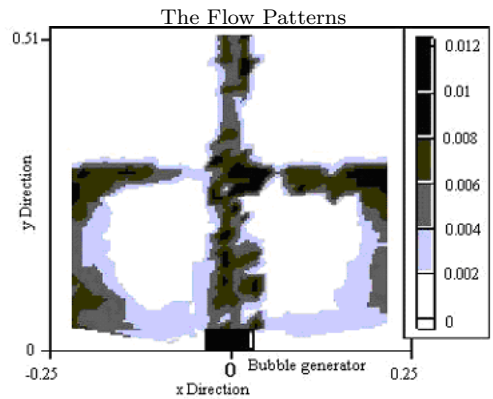

Figure 6. The kinetic energy $(\mathrm{m/s})^2$ for $Q_g = 0.28 \times 10^{-6}$ m^3/s.

The results presented in Figures 3, 4, 5 and 6 confirm the following points:

(1) First, there are two circulating flows of liquid near the bubble plume for both the water and the oil layers. The circulation flows inside the water layer is larger than that inside the oil layer.

(2) The velocity of liquid is high inside the bubble plume in the water layer and near the oil-water interface, while low in other regions.

(3) It is recognized that as the gas flow rate increases, the magnitude of velocity increases and the effective area of the bubble plume (the width of the surface flow) expands in horizontal direction. Here we can recognize two effective areas: the first one is located at the oil-water interface and the second is located on the free surface. Hence, the surface flow of the oil-water interface which is induced by the bubble plume is stronger and larger than that induced in the free surface.

(4) For large gas flow rate values a strong vortex motion is induced inside the deformed area. This vortex motion has a role in generating strong shear stress near the oil-water interface.

(5) The highest kinetic energy is generated at a long distance inside the bubble plume and in the vicinity of the oil-water interface. This observation confirms the idea that the bubble plume can indeed generate a strong and wide surface flow over the bubble generation system.

b) The Mixing Effect

The convection due to the bubble plume inside the oil-layer is different from thermal convection. In the case of thermal convection (Lower Dragging Mode, Viscous Coupling, Upper Dragging Mode and Convection induced by a bubble plume in a thermal stratified liquid, Degen *et al.* 1998, Johnson *et al.* 1997, Johnson & Narayanan 1998, Renardy & Stoltz 2000, Murai *et al.* 2000) oil has an opposite circulation to that of water. Therefore, the oil-water interface is quite stable, because the flow in the vicinity of oil-water interface has the same direction; hence, there is no strong shear stress acting on the interface. On the contrary, the flow for bubble-convection case close to the interface is counter-current. Thus, The flow at the interface is outwards in the water, and inwards in the oil, and hence opposing for

bubble convections as shown in Figure 4. Hence, the interface becomes unstable and has large displacements, especially when the gas flow rate increases since the direction of the two flows inside the oil and the water are opposite to each other. Another reason is the strong local momentum interaction between the bubbles and the liquid. This phenomenon enhances the mixing of the two liquid layers due to the bubble plume.

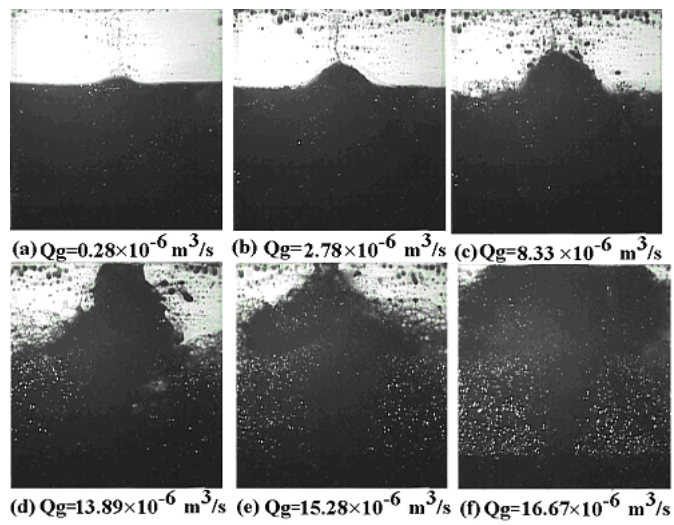

Figure 7. Phase distributions versus gas volume flow rate.

The maximum speed of the surface flow induced by a bubble plume is governed by the flow structure in the initial region where the rising flow changes into a surface flow. Figure 7 shows the photographs of flow visualization in a well-developed stage. Black ink is injected into the water phase in order to identify the interface between the oil and the water layers. The experimental observation of these images clarifies the following points:

(1) Due to the penetration of the bubbles through the interface the oil-water interface upheaves in the center part when a small gas flow rate is given as shown in Figure 7 (a), (b), (c) with parameters $Q_g \leq 12.50 \times 10^{-6}$ m^3/s, $D \leq 2.3$ mm and $\alpha \leq 0.16$. In this case the bubbles enter and penetrate the oil stratum and reach the upper free surface, while the water does not. Moreover, some bubbles accumulate in the vicinity of the oil-water interface and then start to float slowly through the oil around the center part.

(2) The oil layer is separated by the rising water in the center part and descends downwards when a large gas flow rate is provided as shown in Figure 7 (d) and (e) with parameters $Q_g \leq 15.28 \times 10^{-6}$ m^3/s, $D \leq 2.8$ mm and $\alpha \leq 0.19$.

(3) The oil layer is broken and completely destroyed by the strong convection when larger gas flow rates are given with parameters $Q_g = 16.67 \times 10^{-6}$ m^3/s, $D = 3.0$ mm and $\alpha = 0.20$ as shown in Figure 7 (f). The power efficiency of breaking the oil layer in this case is calculated by dividing the potential energy of the interface by the buoyancy energy of injected the bubbles. This efficiency is about 50% to 65%. We can therefore say that the oil layer is easily broken and destroyed by bubbles. This confirms that

the oil stratum can be separated by a bubble plume when the bubble plume has high void fraction and high gas flow rate.

In order to quantitatively explain the mixing effect the following dimensionless cross-correlation coefficient (cc) is defined as:

$$cc = \frac{\int_0^{0.6} \phi_1 \phi_2 \, dxdy}{\sqrt{\int_0^{0.6} \phi_1^2 \, dxdy \int_0^{0.6} \phi_2^2 \, dxdy}} \tag{2}$$

The cross-correlation coefficient (cc) is calculated for 120 consecutive images (4 seconds) and for a range of gas flow rates as shown in Figure 8. From this figure, it is clear that the cross-correlation coefficient decreases when the gas flow rate increases. The oil layer is broken and completely destroyed by the bubble plume at $cc = 0.913$ with the parameters $Q_g = 16.67 \times 10^{-6}$ m^3/s, $D = 3.0$ mm and $\alpha = 0.20$. Figure 9 shows the standard deviation of the cross-correlation coefficient. From this figure we recognize that the maximum fluctuation takes place at $Q_g^* = 8.333$ ($Q_g = 12.50 \times 10^{-6}$ m^3/s). This fluctuation is related to the unsteady flow due to the rising water and bubbles to the free surface and separating of the oil layer. The difference between the two fluids in density and viscosity causes a very unsteady interface motion especially at large gas flow rates. The vortex motion, which is strongly induced for large gas flow rates, plays a role in causing this fluctuation.

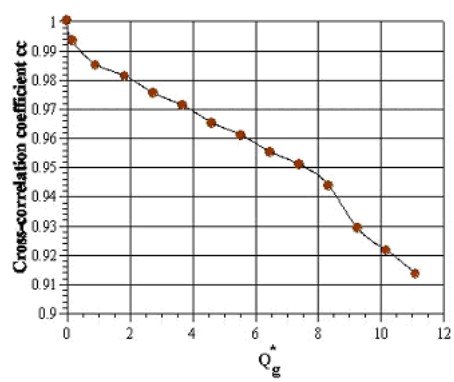

Figure 8. The relationship between the time averaged cross-correlation coefficient cc and Q_g^*.

c) Calculating the Altitude of the Upheaval Bulge of the Two-Phase Stratified Liquid Interface which is Induced by the Bubble Plume

We measured Δh experimentally by using image processing of 600 consecutive images (20 seconds) as shown in Figure 10 (the relationship between the time-averaged measurements of Δh and Q_g^*). This figure shows that Δh increases when the gas flow rate increases and at $Q_g^* = 9.259$, Δh becomes constant. Here Δh reaches its maximum the height of the free surface (0.15 m), and the oil layer is broken and destroyed by the strong bubble convection. Figure 11 shows the relationship between the standard deviation of Δh and Q_g^*. The large fluctuation takes place at $Q_g^* = 8.333$ where Δh reaches its maximum i.e. the height of the free surface (0.15 m). This fluctuation is related to the instability of the oil-water interface

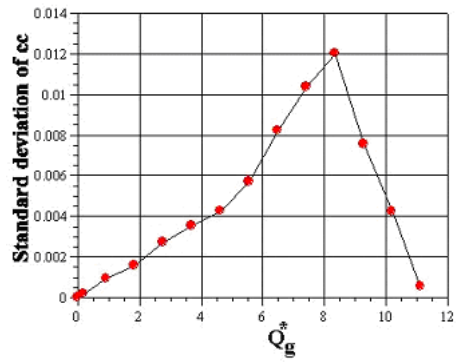

Figure 9. The relationship between the standard deviation of cross-correlation coefficient and $Q - g^*$.

due to the difference between the two fluids in density and viscosity for large gas flow rate values and due to the rising of water and bubbles which penetrate and separate the oil layer up to the free surface. The above results show that Δh is a very important factor (parameter) since it plays an important role in breaking and destroying the oil layer.

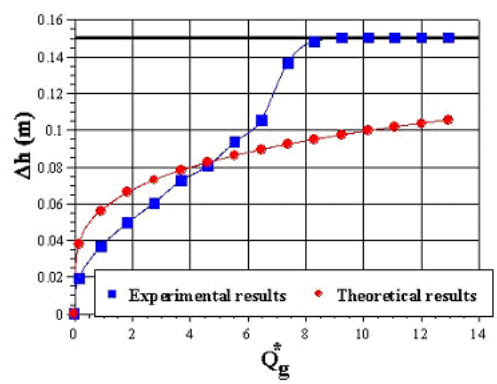

Figure 10. Figure 10: Comparison between experimental results and theoretical results.

In order to explain the variation of Δh quantitatively we can say that the potential energy due to gravity is equal to kinetic energy.

$$(\frac{1}{2}w\delta\,\Delta h)(\rho_1 - \rho_2)g = \frac{1}{2}\rho_1(\frac{Q_l}{w\delta})^2(w\delta) \tag{3}$$

where w is a function of the gas flow rate and shown in Eq. (4) below

$$w = cQ_g^d. \tag{4}$$

Here c and d are constants to be obtained from experimental results. Now, Figure 12 shows the relationship between w and gas flow rate, which is calculated for 120 consecutive images

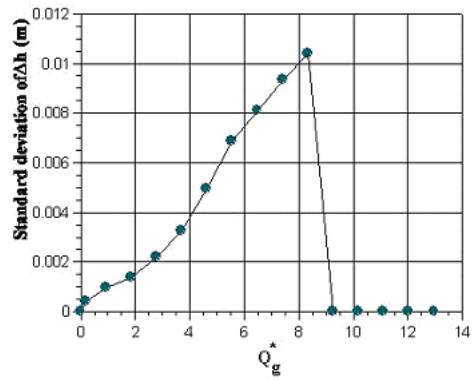

Figure 11. The relationship between the standard deviation of Δh and Q_g^*.

(4 seconds) by using the NIH software. From this figure, c and d are obtained as $c = 1.5$ and $d = 0.7$.

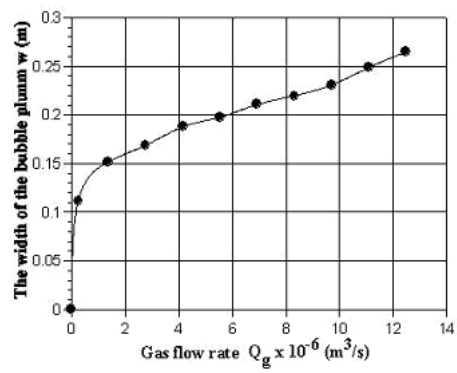

Figure 12. The relationship between w and Q_g.

Also Q_l is a function of gas flow rate taken from Leitch & Baines (1989) as shown below in Eq. (5)

$$Q_l = aQ_g^b. \tag{5}$$

Depending on the above values Δh can be given as follows

$$\Delta h = AQ_g^B, \tag{6}$$

where

$$A = \frac{\rho_1 a^2}{(c\delta)^2(\rho_1 - \rho_2)g}, \qquad B = 2b - 2d. \tag{7}$$

Here A and B are constants to be obtained by using the least-squares (LSA) method.

Fitting gives,

$$\Delta h = 1.454 Q_g^{0.242}, \tag{8}$$

as the theoretical equation for calculating the altitude of the upheaval bulge of the two-phase stratified liquid interface, which is induced by the bubble plume. Here, Δh is calculated by using Eq. (8). Figure 10 shows the results of the experimental measurements and the theoretical calculations of Δh. This figure shows that the experimental results agree with the theoretical results for $Q_g^* \leq 6.481$ ($Q_g \leq 9.72 \times 10^{-6}$ m^3/s) but not for values of Q_g^* larger than 6.481 ($Q_g > 9.72 \times 10^{-6}$ m^3/s). The reasons of this discrepancy are related to the following points:

(1) The experimental results are limited to $Q_g^* \leq 9.259$ where Δh reaches its maximum i.e. the height of the free surface in the tank (0.15 m).
(2) The difference between two fluids in density and viscosity causes a very unsteady interface motion especially for large gas flow rates. Then the flow in the tank becomes unsteady.
(3) The penetration of water is not only governed by the momentum of the water jet but also by the vortex motion inside the deformed area. The vortex motion actually generates strong shear stress near the oil-water interface.
(4) The effect of the viscosity of oil, which quickly decreases the bubble speed when bubbles enter the oil layer. Therefore, the void fraction inside the oil increases. Hence, the mixing becomes more difficult due to the buoyancy in the oil-layer.
(5) The effect of wavy oscillation of the oil-water interface, which is caused by the liquid.

4. CONCLUDING REMARKS

Flow visualization of the bubble plume in two immiscible stratified fluids is carried out in order to improve the applicability of the bubble plume as an oil fence. The covering effect of the oil layer on the free surface and the influence of the convection due to the bubble plume are investigated by using image processing and PIV measurements. It is confirmed by the present research that the flow structure is sensitively modulated by the gas flow rate. The main results can be summarized as follows

(1) The PIV measurements and the pathlines measurement results of the internal flow structure of the immiscible two-phase stratified liquids show that the velocity of the surface flow induced by the bubble plume in the vicinity of the oil-water interface is larger and stronger than that inside the oil layer. Moreover, the surface flow is particularly rapidly generated in the vicinity of the oil-water interface.
(2) The highest kinetic energy is generated at a far distance inside the bubble plume and in the vicinity of the oil-water interface. This observation confirms the idea that the bubble plume can generate a strong and wide surface flow over the bubble generation system.
(3) The oil layer is easily broken by bubbles. It is confirmed that the oil stratum can be separated by a bubble plume when the bubble plume has high void fraction and high gas flow rates.
(4) The altitude Δh of the upheaval bulge of the two-phase stratified liquid interface which is induced by the bubble plume (which plays an important role in breaking and

destroying the oil layer) is measured experimentally and calculated theoretically. The experimental results agree with the theoretical result up to a certain limit.

References

1. Earnshaw, P.B. and Lawford, J.A. (1966) Low-Speed Wind Tunnel Experiments on a Series of Sharp-Edged Delta Wings, ARC R&M No. 3424. Abdulmouti, H., Murai, Y., Ohno, Y. and Yamamoto, F. (2001) Measurement of Bubble Plume Generated Surface Flow Using PIV, *Journal of the Visualization Society of Japan*, **21** (2), 31–37.
2. Gross, R.W. and Kuhlman, J.M. (1992) Three-Component Velocity Measurements in a Turbulent Recirculating Bubble-Driven Liquid Flow, *Int. J. Multiphase Flow*, **18**, 413–421.
3. Sun, T.Y. and Faeth, G.M. (1986a) Structure of Turbulent Bubbly Jets–I. Methods and Centerline Properties, *Int. J. Multiphase Flow*, **12**, 99–114.
4. Sun, T.Y. and Faeth, G.M. (1986b) Structure of Turbulent Bubbly Jets–II. Phase Property Profiles, *Int. J. Multiphase Flow*, **12**, 115–126.
5. Hussain, N.A. and Narang, B.S. (1984) Simplified Analysis of Air-Bubble Plumes in Moderately Stratified Environments, *ASME Journal of Heat Transfer*, **106**, 543–551.
6. Hara, S., Ikai, M. and Namie, S. (1984) Fundamental Study on an Air Bubble Type of Oil Boom, *Trans. Ship-Making Society of Kansai-Japan*, 194.
7. Chesters, A.K., Van Doorn, M. and Goossens, L.H.J. (1980) A General Model of Unconfined Bubble Plumes from an Extended Source, *Int. J. Multiphase Flow*, **6**, 499–521.
8. McDougall, T.J. (1978) Bubble Plumes In Stratified Environments, *Journal of Fluid Mechanics*, **85**, 655–672.
9. Abdel-Aal, H.K., Stiles, G.B. and Holland, C.D. (1966) Formation of Interfacial Area at High Rates Gas Flow Through Submerged Orifices, *AICHE J.*, **12**, 174–180.
10. Degen, M.M., Colovas, P.W. and Andereck, C.D. (1998) Time-Dependent Patterns in the Two-Layer Rayleigh-Benard System, *Phys. Rev. E*, **57**, 6647–6659.
11. Johnson, D., Narayanan, R., Dauby, P.C. (1997) Geometric Effects on Convective Coupling and Interfacial Structures in Bilayer Convection, *Phys. Rev. E*, **56**, 5462–5472.
12. Johnson, D. and Narayanan, R. (1998) Marangoni Convection in Multiple Bounded Fluid Layers and its Application to Materials Processing, *Phil. Trans. R. Soc. Lond A*, **356**, 885–898.
13. Renardy, Y.Y. and Stoltz, C.G. (2000) Time-Dependent Pattern Formation for Convection in Two Layers of Immiscible Liquids, *Int. J. of Multiphase Flow*, **26**, 1875–1889.
14. Kataoka, I., Serizawa, A. and Besnard, D.C. (1993) Prediction of Turbulence Suppression and Turbulence Modeling in Bubbly Two-Phase Flow, *Nuclear Engineering and Design*, **141**, 145–158 (North-Holland).
15. Murai, Y. and Matsumoto, Y. (1998) Numerical Analysis of Detailed Flow Structures of a Bubble Plume, *JSME International Journal, Series B*, **41** (3), 568–575.
16. Matsumoto, Y. and Murai, Y. (1995b) Numerical Simulation of Bubble Plume in a Tank with Free Surface, *Trans. Japan. Soc. Mech. Eng.*, **61**, 588, 54–61.
17. Murai, Y. and Matsumoto, Y. (1999) Eulerian Analysis of Bubbly Two-Phase Flows Using CIP Scheme, *Computational Fluid Dynamics Journal*, **8** (1).
18. Kimura, I., Kimura, H. and Takamori, T. (1986) Image Processing of Flow around a Circular Cylinder by Using Correlation Techniques, *Proc. 4th Int. Int. Symp. Flow Visualization*, Hemisphere, 221–226.
19. Murai, Y., Ohno, Y., Bae, D.S., Abdulmouti, H. and Yamamoto, F. (2001) Bubble-Generated Convection in Immiscible Two-phase Stratified Liquids, *Proceedings of ASME FEDSM*, May 29–June 1, (18180), New Orleans, U.S.A.
20. Leitch A.M. and Baines W.D. (1989) Liquid Volume Flux in a Weak Bubble Plume, *J. Fluid Mech.*, **205**, 77–98.